Integrating Time-Series Meteorological Data and sUAS Information into a Machine Learning Framework for California Vineyard Water Stress Monitoring

Rui Gao
Utah State University
Maria Mar Alsina
Institute of Research, Technology, Food & Agriculture (IRTA)
Alfonso Torres-Rua
alfonso.torres@usu.edu

Utah State University
Lawrence Hipps
Utah State University
William P. Kustas
U.S. Department of Agriculture, Agricultural Research Service
Martha Anderson
U.S. Department of Agriculture, Agricultural Research Service
Hector Nieto
Institute of Agricultural Sciences
Andrew J. McElrone
USDA-Agricultural Research Service
Kyle Knipper
U.S. Department of Agriculture Agricultural Research Service
Nicolas Bambach
University of California, Davis
Sebastian J. Castro
U.S. Department of Agriculture Agricultural Research Service
John H. Prueger
U.S. Department of Agriculture Agricultural Research Service
Joseph Alfieri
U.S. Department of Agriculture Agricultural Research Service
Lynn G. McKee
U.S. Department of Agriculture, Agricultural Research Service

William A. White
U.S. Department of Agriculture, Agricultural Research Service
Feng Gao
U.S. Department of Agriculture, Agricultural Research Service
Calvin Coopmans
Utah State University
Ian Gowing
Utah State University
Nurit Agam
Ben-Gurion University of the Negev
Luis Sanchez
Gallo Viticulture Research
Nick Dokoozlian
Gallo Viticulture Research

Research Article

Keywords: Leaf water potential, crop water stress, sUAS imagery, Machine learning, California vineyards

Posted Date: November 13th, 2025

DOI: https://doi.org/10.21203/rs.3.rs-7952103/v1

Additional Declarations: No competing interests reported.

Version of Record: A version of this preprint was published at Irrigation Science on March 14th, 2026. See the published version at https://doi.org/10.1007/s00271-026-01102-8.

Integrating Time-Series Meteorological Data and sUAS Information into a Machine Learning Framework for California Vineyard Water Stress Monitoring

Rui Gao[a,b], Maria Mar Alsina[c], Alfonso F. Torres-Rua[a*], Lawrence Hipps[d], William P. Kustas[e], Martha Anderson[e], Hector Nieto[f], Andrew J. McElrone[g,h], Kyle Knipper[i], Nicolas Bambach Ortiz[h,i], Sebastian J. Castro[i], John H. Prueger[j], Joseph Alfieri[i], Lynn G. McKee[e], William A. White[e], Feng Gao[e], Calvin Coopmans[k], Ian Gowing[a], Nurit Agam[l], Luis Sanchez[m], and Nick Dokoozlian[m]

[a]Civil and Environmental Engineering Department, Utah State University, Old Main Hill, Logan, UT 84322, USA

[b]Civil and Environmental Engineering Department, University of California, Merced, CA 95340, USA

[c]Institute of Research, Technology, Food & Agriculture (IRTA), Mas Badia. Tallada d'Empordà, 17134, Spain

[d]Plants, Soils, and Climate Department, Utah State University, Old Main Hill, Logan, UT 84322, USA

[e]U.S. Department of Agriculture, Agricultural Research Service, Hydrology and Remote Sensing Laboratory, Beltsville, MD 20705, USA

[f]Institute of Agricultural Sciences – CSIC, 28006 Madrid, Spain

[g]Crops Pathology & Genetics Research Unit, USDA-Agricultural Research Service, Davis, CA 95616, USA

[h]Department of Viticulture & Enology, University of California Davis, Davis, CA 95616, USA

[i]Sustainable Agriculture Water Systems Research Unit, USDA ARS, Davis, CA 95616, USA

[j]U.S. Department of Agriculture, Agricultural Research Service, National Laboratory for Agriculture and The Environment: Ames, IA 50011, USA

[k]Electrical and Computer Engineering Department, Utah State University, Old Main Hill, Logan, UT 84322, USA

[l]Jacob Blaustein Institutes for Desert Research, Ben-Gurion University of the Negev, Sde-Boqer Campus 84990, Israel

[m]Gallo Viticulture Research, Modesto, CA 95354, USA

[*]alfonso.torres@usu.edu

Abstract: Efficient irrigation management is fundamental to sustainable crop production, particularly under increasing temperatures and limited water availability. In vineyards, water stress significantly influences grapevine development and productivity. Controlled water stress is intentionally applied in deficit-irrigated systems to regulate yield and enhance fruit quality. Therefore, vineyards must be routinely monitored to prevent excessive stress that could cause detrimental effects. In this study, we developed a machine-learning framework based on the eXtreme Gradient Boosting (XGB) machine-learning model to estimate grapevine leaf water potential (Ψ_{leaf}) using meteorological data and high-resolution imagery from small unmanned aerial systems (sUAS) over commercial vineyards of different varieties and in different climatic zones in California. The framework incorporates key meteorological and image-derived features, including maximum air temperature in the 24 hours prior to the flight, air temperature at the time of flight, the difference between these two temperatures, as well as canopy temperature derived from sUAS thermal imagery. These features were included to indirectly capture plant-water-weather interaction during the 24-hour period preceding data collection, enhancing the model's practical applicability. The XGB model demonstrated robust performance, achieving an RMSE of 0.16 MPa, a bias of -0.06 MPa, and a correlation coefficient of 0.83 while minimizing computational cost. Model generalizability was further validated in an independent vineyard, demonstrating its potential for commercial application in precision irrigation and vineyard water management. Our research highlights the potential for broader applicability, particularly in addressing flash drought and promoting adaptive water resource management.

Keywords: Leaf water potential; crop water stress; sUAS imagery; Machine learning; California vineyards.

1. Introduction

California's Central Valley, one of the most productive agricultural regions worldwide, generates more than $40 billion annually in crops (Grantham & Viers, 2014; Mitchell et al., 2016). Under a semiarid climate where increasing temperatures, declining water allocations, and intensified evaporative demand are projected to further constrain irrigation supplies (Bonada & Sadras, 2015; Diffenbaugh et al., 2011; Nicholas & Durham, 2012; Viers et al., 2013). Maintaining grape yield and fruit quality while reducing water consumption has therefore become a central challenge for sustainable vineyard management (Kustas et al., 2019). Under projected warming and limited water availability, precise irrigation scheduling based on actual vine water status is essential to sustain productivity, optimize fruit composition, and conserve regional water resources (Chaves et al., 2010; Hannah et al., 2013). As a high-value perennial crop, grapevine represents both an economic and environmental priority for improved irrigation efficiency in water-limited regions (Diffenbaugh et al., 2011; Nicholas & Durham, 2012).

Grapevine water stress governs gas exchange, berry composition, and overall vine productivity (Miras-Avalos & Araujo, 2021). Moderate stress at the ripening stage enhances sugar and anthocyanin concentration, whereas severe or early stress substantially reduces yield and berry quality (Albrizio et al., 2023; Bravdo et al., 1985). Because of these physiological links, vine water potential—expressed as leaf (Ψ_{leaf}) or stem (Ψ_{stem}) water potential—serves as a direct physiological indicator of the plant's water status and irrigation need. These metrics integrate soil moisture, atmospheric demand, and plant hydraulic regulation, providing a robust framework for understanding vine–atmosphere coupling and irrigation demand (Sperry, 2000).

Despite their reliability, conventional pressure-chamber measurements of Ψ_{leaf} or Ψ_{stem} remain labor-intensive, destructive, and time-consuming, making them impractical for frequent or large-scale monitoring (Abbatantuono et al., 2024). Spatial variability in soil texture, vine vigor, and canopy architecture across vineyard blocks further limits the representativeness of point-based measurements (Alliaume et al., 2024; Ferro et al., 2023). Consequently, irrigation scheduling often relies on sparse sampling or indirect indicators that fail to capture fine-scale heterogeneity in vine water status (Abbatantuono et al., 2024). The need for cost-effective, spatially continuous, and non-destructive methods to monitor grapevine water stress has become increasingly urgent, particularly under dynamic environmental conditions and spatially variable vineyard microclimates.

Advances in remote sensing and machine learning technologies offer an effective pathway to overcome these limitations. The satellite platform provides promising grapevine water stress estimation, considering the technical progress in the spatial and temporal resolution improvement; the small unmanned aerial systems (sUAS) provide excellent estimations since they can obtain high-resolution images (Abbatantuono et al., 2024). At high spatial resolution, products such as the volume and biomass of individual grapevines can be generated by isolating the vine canopy from the interrow (Aboutalebi et al., 2019; Gao et al., 2021, 2022, 2023; Gao & Torres-Rua, 2023).

Many research have demonstrated the success of using the combination of high-resolution sUAS information and machine learning for vine water stress estimation. For example, Poblete et al. (2017) built artificial neural network (ANN) models for vine Ψ_{stem} estimation at a drip-irrigated Carmenere vineyard in Talca, Maule Region, Chile, aiming to address the highly nonlinear relationships between spectral reflectance and vine water stress. Their findings demonstrated that drone-mounted multispectral cameras could effectively capture the spatial variability in vine water stress, with the ANN models performing best when incorporating spectral bands at 550, 570, 670, 700, and 800 nm. Validation analysis indicated that the ANN model could estimate Ψ_{stem} with a mean absolute error (MAE) of 0.1 MPa, root mean square error (RMSE) of 0.12 MPa, and relative error (RE) of -9.1%. Laroche-Pinel et al. (2024) used UAV-mounted Near InfraRed (NIR) and Short-Wave Infrared (SWIR) hyperspectral cameras (900 – 1700 nm) combined with machine learning models to estimate Ψ_{stem} in a vineyard, achieving an R^2 at 0.54 and RMSE at 0.11 MPa, underscoring the efficacy of fine-resolution hyperspectral imagery for vineyard water stress assessment.

Among the recent efforts, the study by Tang et al. (2022) is particularly noteworthy and forms a conceptual foundation for the present research. Tang et al. (2022) demonstrated the potential of integrating sUAS-derived information with meteorological data from nearby weather stations located approximately 12 and 20 km away, recorded at the time of the flight, for Ψ_{leaf} estimation. Using a Random Forest (RF) model, they achieved an R^2 of 0.78, RMSE of 0.12 MPa, and MAE of 0.10 MPa in a vineyard. The critical role of meteorological data was emphasized, particularly air temperature and vapor pressure deficit at the time of image acquisition, in the model's predictive performance. These results highlight the effectiveness of integrating proximal weather information with high-resolution imagery for vine water stress estimation. Despite this progress, the study by Tang et al. (2022) also leaves open several important avenues for further investigation. First, the reliance on weather data from stations located several kilometers away introduces potential spatial mismatches between recorded and actual vineyard microclimates, warranting closer examination of their impact on model accuracy. Second, their trained models were developed under specific site conditions and sensor configurations, suggesting a need to evaluate model transferability across different vineyards, spatial resolutions, and environmental contexts. Third, their work raises the question of whether meteorological conditions in the hours or days preceding image acquisition might influence Ψ_{leaf} at the time of flight.

The Grape Remote sensing Atmospheric Profiling and Evapotranspiration eXperiment (GRAPEX) project (Kustas et al., 2018, 2019) started in 2013 and included field data collection campaigns in vineyards across California for several years, including Ψ_{leaf} and Ψ_{stem} measurements, meteorological data, and high-resolution sUAS images collected by the AggieAir platform[1] at Utah State University. GRAPEX captured hydrological, physiological, and meteorological conditions across multiple vineyard blocks and varieties, multiple growing seasons, and climate regions, which provides a unique resource to explore those three investigations.

The primary objective of this research is to evaluate the feasibility of using a high-resolution sUAS imagery combined with time-series meteorological data from local sensors to spatially estimate grapevine water stress. Additionally, this study aims to develop a more robust and transferable methodology that can be adapted to diverse vineyard varieties across California's Central Valley. By addressing limitations in spatial variability, sensor specificity, and model generalizability, the research seeks to advance scalable approaches for field-level monitoring of grapevine water stress.

2. Materials and Methods

2.1 Site description and vine water stress measurements

Four commercial vineyards situated in three different climatic regions across California, as illustrated in Figure 1, were included in this study. The vineyard blocks BAR012 and BAR007, planted to *Vitis vinifera* cv. Cabernet Sauvignon and cv. Petite Sirah, respectively, were the furthest north in Sonoma County, south of Cloverdale, CA. The SLM vineyard, planted to *Vitis vinifera* cv. Pinot Noir, was situated around 20 km northeast of Lodi, CA in the California Central Valley. Lastly, the RIP 720 vineyard, planted to *Vitis vinifera* cv. Merlot, was situated around 30 km west of Fresno, also in the California Central Valley. The RIP 760 vineyard, geographically proximate to the RIP 720 vineyard, was not included in the model generation and was utilized as a test location (blind test) to validate the model's performance.

In all these locations, the vines were trained in a horizontally split canopy system, with rows separated ~3.35 m. The distance between vines was ~1.83 m in the Sonoma locations and ~1.52 m in the Central Valley Locations. The white "×" symbols in Figure 1 indicate the specific locations within each block where the Ψ_{leaf}/Ψ_{stem} measurements were taken periodically, over the course of multiple seasons along

[1] https://uwrl.usu.edu/aggieair/

with sUAS flights. The white "×" symbol highlighted by the black square represents the sample used to test the machine learning model performance. Details will be presented in the section 2.4.2.

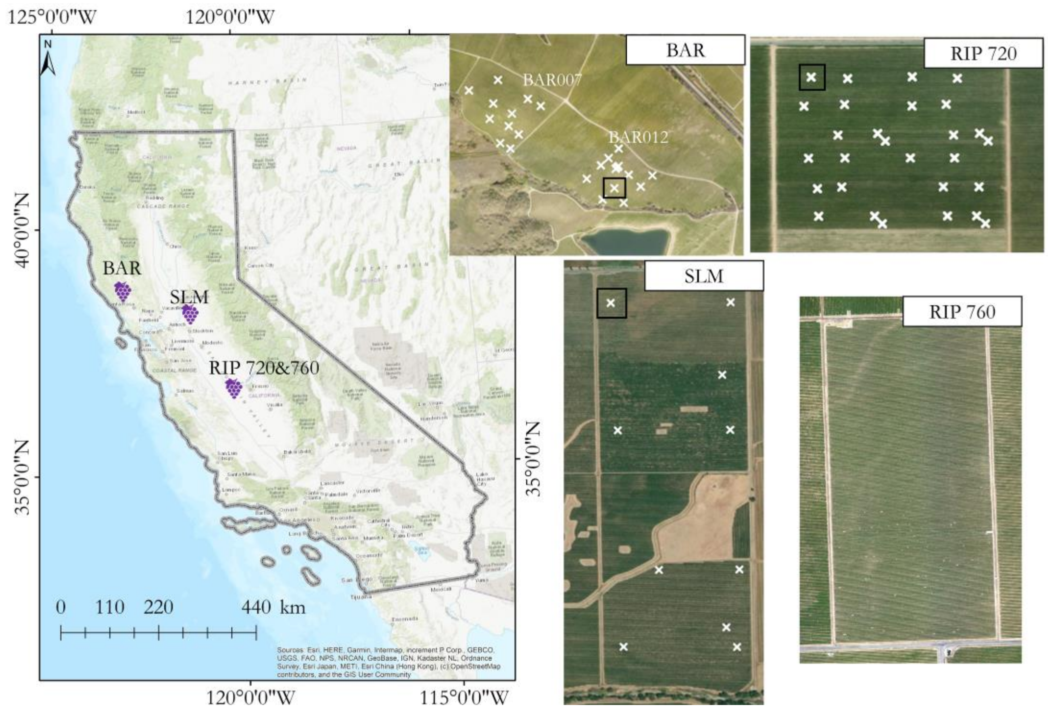

Figure 1. GRAPEX vineyard blocks in California showing specific Ψ_{leaf}/Ψ_{stem} sampling sites (×). The samples highlighted by the black square represent the sample used to test the performance of machine learning model performance. The corresponding information is not included in the machine learning training dataset. RIP 760 is treated as a blind test location.

Both Ψ_{leaf} and Ψ_{stem} were measured during sUAS overflights at the sites identified in Figure 1. The Ψ_{leaf} measurements were conducted on fully expanded leaves fully exposed to sunlight. The leaves were enclosed in a plastic bag, detached from the vine, and their water potential was immediately measured using a pressure chamber (Turner and Long 1980). In each experimental site, there were from nine to twelve predetermined sampling locations consisting of around four meters of vine canopy along the vine row (two adjacent vine spaces of either 1.5 m in RIP and SML or 1.8 m in BAR). These locations were the same for all the sampling times representing different levels of vine water status at the site and are located strategically in the vineyard block. Two or three researchers working in parallel and moving on small all-terrain vehicles could sample all the locations in less than one hour. One sample consisted of an average of three to five leaves per sampling location, and between six and twelve samples per block were collected at different sampling locations under each overflight, depending on the vineyard site and the available resources on a specific date and time. The exact position of each measured leaf within the canopy was not recorded, as identifying individual leaves during measurement was impractical. Instead, the mean value from three to five leaves was assigned to the corresponding canopy section. Three researchers worked simultaneously to ensure representative conditions during image collection, minimizing the time between samples. Ψ_{stem} measurements followed a similar procedure, with the leaf being placed in a small opaque bag for around half an hour before measurement. The number of samples for both Ψ_{stem} and Ψ_{leaf} for each flight is shown in Table 1.

Table 1. The number of Ψ_{leaf} and Ψ_{stem} measurements and corresponding AggieAir flights over four different California vineyards between 2015 and 2019. "√" under the "EC tower" column indicates the available EC-flux tower data.

Site name	Date	EC tower	Ground measurements		AggieAir sUAS flights*
			Ψ_{leaf}	Ψ_{stem}	
SLM	6/2/2015	√	20	0	2
	7/11/2015	√	15	0	2
BAR007	6/27/2019	√	11	8	2
	7/29/2019	√	17	12	2
BAR012	8/8/2017	√	10	0	1
	8/9/2017	√	10	0	1
	6/27/2019	√	15	13	3
	7/29/2019	√	25	12	2
	7/30/2019	√	17	11	3
RIP720	6/19/2018	√	36	12	3
	7/13/2018	√	48	0	2
	8/5/2018	√	8	4	2
	8/6/2018	√	22	10	1
	5/4/2019	√	9	5	1
Total			263	87	

* Number of flights at around Landsat overpass, local solar noon, and mid-afternoon.

Williams and Araujo (2002) reported a linear relationship between Ψ_{leaf} and Ψ_{stem}, which was also observed in the GRAPEX dataset (Figure 2). A linear regression line (R^2=0.73 and RMSE=0.07 MPa) was generated based on the pair of Ψ_{leaf}/Ψ_{stem} measurements. Thus, instead of considering both Ψ_{leaf} and Ψ_{stem}, all modeling, analysis, and mapping presented in this manuscript focus on Ψ_{leaf}.

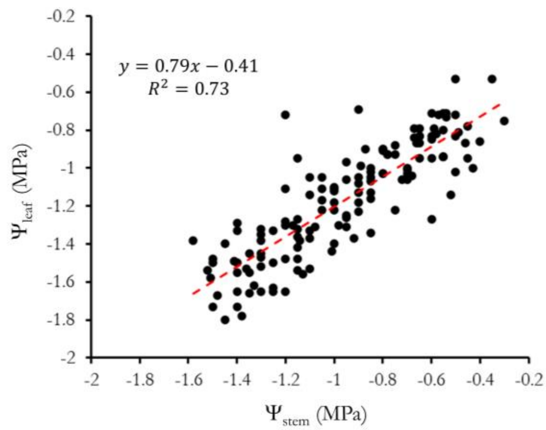

Figure 2. Linear relationship between measured Ψ_{leaf} and Ψ_{stem} based on the available dataset from commercial vineyards in California.

2.2 sUAS data

High-resolution images gathered via the AggieAir sUAS platform between 2015 and 2019 were used in this study. Details of the data are presented in Nassar et al. (2021). These data include four-band spectral images: Blue (B), Green (G), Red (R), and Near-infrared (NIR) with similar spectral response to Landsat 8 as well as calibrated microbolometer thermal imagery. The flight details, including the date, number of flights, and corresponding ground measurements, are provided in Table 1.

2.3 Meteorological data

All the GRAPEX experimental sites were instrumented to monitor the local meteorological conditions with full eddy-covariance (EC) systems. Six meteorological variables measured every hour within a two-week time-series window per sUAS flight were used in this study: air temperature (T_a in ºC), vapor pressure deficit (VPD in kPa), actual vapor pressure (e_a in kPa), carbon dioxide density (CO_2 in mg·m^{-3}), net radiation (R_n in Wm^{-2}), and relative humidity (RH in %). Therefore, a total of 2016 (6 variables × 14 days × 24 hours) hourly features (potential predictors) per sUAS flight were evaluated for all the sUAS flights.

A small portion of the meteorological dataset (approximately 1%) was missing due to factors such as battery interruptions. Missing values were filled using the mean of available observations for the same hour within a 14-day moving window. For example, if air temperature at 10:00 a.m. on Day 14 was unavailable, the average of valid 10:00 a.m. readings from the preceding thirteen days was used as the replacement.

2.4 Ψ_{leaf} sample extending

2.4.1 Basis for increasing the number of samples of Ψ_{leaf}

We proposed a methodology to extend the number of Ψ_{leaf} samples for running the ML model. The basis lies in the homogeneous canopies around the target vine.

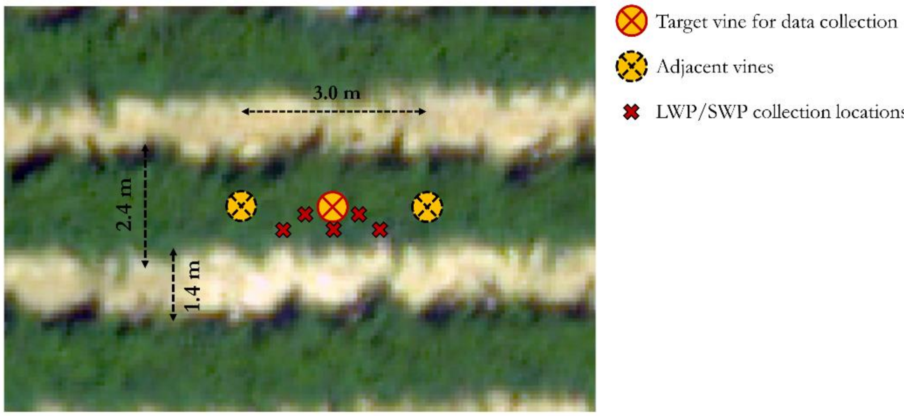

Figure 3. An example showing the field Ψ_{leaf} measurements. The background image comes from the AggieAir sUAS platform on June 19th, 2018 (11:20 am) at RIP720. The red cross cycle symbol represents the target data vine for Ψ_{leaf} collection, and the black dash-lined cross cycle symbol represents the target vine's adjacent vines. Five bold red crosses represent five sample leaves where the researchers took Ψ_{leaf} measurements.

The vine canopy width in July is around 2.4 m (Figure 3). The distance between two adjacent vines in the same row is ~1.5 m. The averaged Ψ_{leaf} value is considered to represent the water status for the single vine (i.e., the target vine in Figure 3). Considering the similarity of the neighboring vines (same variety, canopy management, soil, fertilization, and irrigation conditions), the Ψ_{leaf} measurement then represents the condition of the vines within an area, such as a 3.0 m by 2.4 m rectangle area (Figure 3).

2.4.2 Sample extending algorithm based on sUAS imagery

The AggieAir sUAS platform provided imagery with different pixel resolutions, with the highest resolution being 0.15 m for the multispectral images and 0.60 m for the temperature images. Based on these characteristics, we tested two rectangular domains for analysis. The first domain had dimensions of 3.0 m in length and 2.4 m in width, containing 20 (5×4) 0.6-m pixels (Figure 4 (a)). The second domain had dimensions of 3.0 m in length and 1.8 m in width, containing 15 (5×3) 0.6-m pixels (Figure 4 (b)). Within each 0.6 m temperature pixel, there were 4×4 spectral pixels (R, G, B, and NIR) at a resolution of 0.15 m (Figure 5). The displacement between domains (a) and (b) is 0.30 m north-south between them.

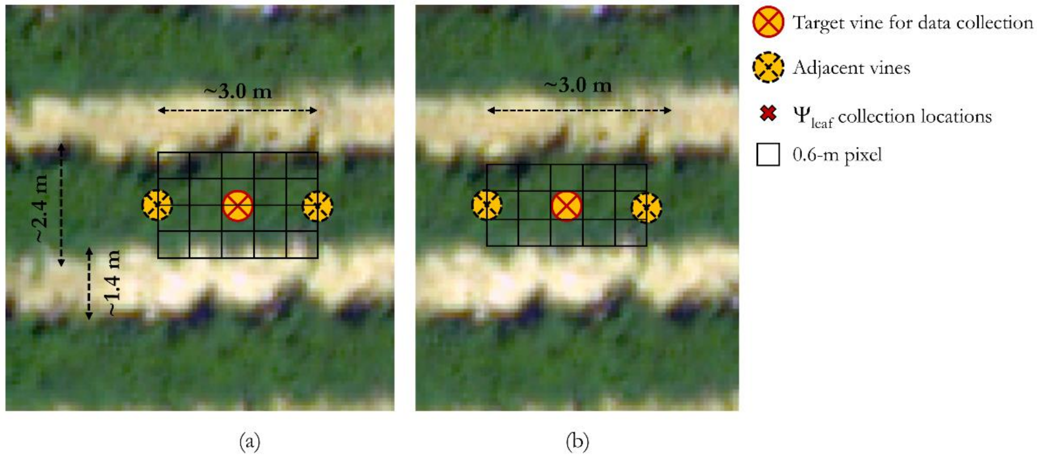

Figure 4. Examples showing how the feature extraction model extends the Ψ_{leaf} samples. (a) Creating a rectangle domain with 3.0 m length and 2.4 m width containing 20 (5×4) 0.6 m pixels. (b) Creating a rectangle domain with 3.0 m length and 1.8 m width containing 15 (5×3) 0.6 m pixels.

All 35 pixels (from two rectangular domains) at 0.6-m resolution were initially assigned the same Ψ_{leaf} value; however, not all pixels were retained for further analysis. Any 0.6-m pixel with a mean NDVI value below 0.65 was excluded. This NDVI threshold was determined based on a manual classification of vine vegetation pixels using optical imagery, as described in a previous GRAPEX study (Gao, Torres-Rua, et al., 2023). The mean NDVI at 0.6 m resolution was calculated by averaging the NDVI values from the corresponding 0.15 m resolution sub-pixels (Figure 5). The remaining valid 0.6-m pixels, those with NDVI $\geq$ 0.65, were all assigned to the same Ψ_{leaf} value. At the end, the Ψ_{leaf} samples were extended from 263 to 2370.

Among the 2370 samples, 153 samples (6.5% of the total) were related to the target vine, which were highlighted by black squares in Figure 1, to test the XGB model performance. 2217 samples (93.5%) were used to train the XGB model. Importantly, the test samples were completely independent of the training dataset, and no information from these samples was used during model development.

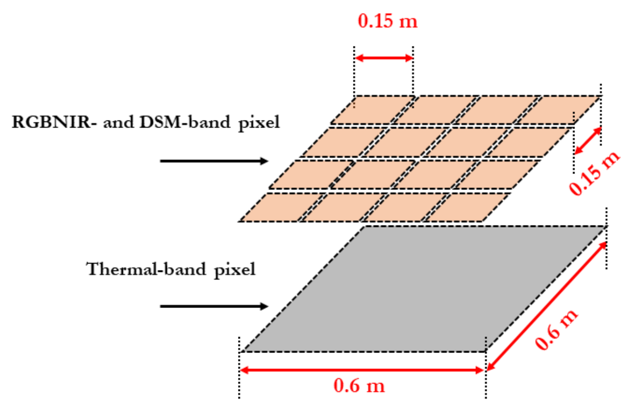

Figure 5. An example: one 0.6 m temperature pixel aligned with a 4×4 0.15 m spectral image (R, G, B, and NIR).

A Python algorithm developed by Gao & Torres-Rua (2025) implements the process described above. This program also generates sixteen sUAS image-based values for each thermal pixel location that will be evaluated for inclusion in the XGB Ψ_{leaf} model, including averaged spectral bands, vegetation indexes (VIs), and temperature. Since only grapevine-vegetation pixels are retained, the 0.6 m temperature pixel is recognized as the canopy (vine-vegetation) temperature (T_c). It is assumed that this feature extraction model can also be applied to other vineyards. In such cases, the NDVI threshold (0.65) needs to be adjusted accordingly.

2.5 Model evaluation metrics

Root mean square error (RMSE), bias, the Pearson correlation coefficient (r), and Willmott's index of agreement (d) were used together to provide a comprehensive assessment of model performance, covering the aspects of accuracy, precision, and agreement with observations. These statistics, along with optional plots such as 1:1 scatter plots, residual plots, and Q–Q plots, are documented in a Python GitHub repository (Gao, 2025), making them easily accessible during code development.

RMSE (Equation 1) can indicate how much the model's predictions deviate from the observations on average. Bias (Equation 2) helps in understanding the systematic tendency of the model to either overestimate or underestimate the observations. r (Equation 3) can indicate the strength and direction of the linear relationship between predicted and observed values. A correlation close to 1 or -1 indicates a strong linear relationship, suggesting that the model can capture the variability of the observations well. d (Equation 4) considers both the mean absolute error and the variability of the observations, showing insight into how well the model replicates the variability and pattern of the observations (Willmott, 1982).

$$RMSE = \sqrt{\frac{\sum_{i=1}^{n}(o_i - \hat{p}_i)^2}{n}} \qquad \text{Equation 1}$$

$$Bias = \frac{1}{n}\sum_{i=1}^{n}(o_i - \hat{p}_i) \qquad \text{Equation 2}$$

$$r = \frac{cov(o,p)}{\sigma_o \sigma_p} \qquad \text{Equation 3}$$

$$d = 1 - \frac{\sum_{i=1}^{n}(o_i - p_i)^2}{\sum_{i=1}^{n}(|p_i - \bar{o}| + |o_i - \bar{o}|)^2} \qquad \text{Equation 4}$$

where o represents observations, o_i is the observed value for the ith observations, $\bar{o}$ is the mean of observations, p represents predictions, p_i is the estimated value for the ith estimations, $\hat{p}_i$ is the estimated value corresponding to the ith observations, n is the number of paired observations.

3. Results

3.1 Meteorological predictor selection

Figure 6 (a) presents the Pearson correlation coefficients quantifying the relationships between Ψ_{leaf} and meteorological variables at different hourly lags (e.g., air temperature eight hours before flight time). The red dashed arrows indicate the empirical threshold ($|r| > 0.6$) adopted in this study to highlight features strongly associated with Ψ_{leaf}. Based on this criterion, 112 out of 2016 tested variables are strongly associated with Ψ_{leaf}. Among these, 42 (38%) correspond to T_a, 37 (33%) to VPD, 26 (23%) to RH, and 7 (6%) to e_a, as shown in Figure 6 (b). These four meteorological variables were therefore selected as potential predictors for Ψ_{leaf} estimation, whereas CO_2 density and R_n were excluded due to weak correlation ($|r| < 0.6$).

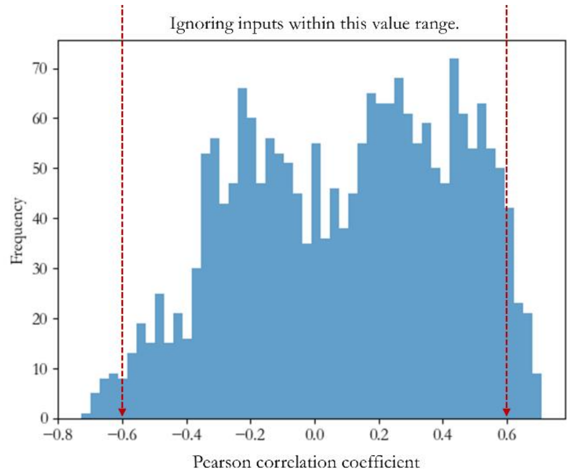

(a)

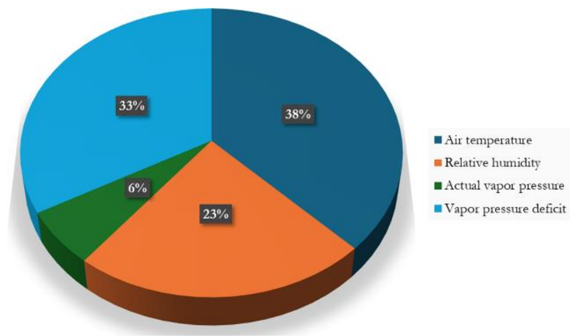

(b)

Figure 6. The Pearson correlation coefficient between meteorological variables and Ψ_{leaf}. (a) The histogram of the Pearson correlation coefficient between the meteorological variable and Ψ_{leaf}. The red dashed arrows indicate the threshold -0.6 and 0.6, respectively. The number of variables with an absolute Pearson correlation coefficient above 0.6 is 112. (b) The percentage of each type of meteorological variable among the 112 identified.

Red circles in Figure 7 denote instances where the absolute Pearson correlation coefficient exceeds 0.6, highlighting periods of strong association between meteorological variables and Ψ_{leaf}. The x-axis represents the sUAS flight index i, with $i-336$ corresponding to 336 hours (two weeks) prior to the flight time. Gray-shaded blocks indicate 24-hour intervals. Among the four meteorological variables analyzed, high-correlation periods were primarily observed within the first, fourth, fifth, thirteenth, and fourteenth 24-hour intervals closest to the flight time (i).

Based on these findings, and to streamline the XGB model, only the hourly T_a, VPD, and RH from the closest 24-hour period were included in the subsequent analysis. e_a was excluded because its strong correlations with Ψ_{leaf} occurred predominantly before this period. Additionally, CO_2 density was incorporated as an exploratory variable to assess the XGB model's capability in handling this rarely measured field parameter.

Including all hourly observations for the four meteorological variables within the 24-hour window would substantially increase the complexity of data collection, processing, and model training. To preserve temporal information while reducing dimensionality, we extracted key features that capture meaningful temporal dynamics. Since most AggieAir flights occurred between 11 a.m. and 3 p.m., we examined the diurnal variation of meteorological variables over 24-hour periods on flight days. Two examples are shown in Figure 8: one flight at 10:41 a.m. on 6 August 2018 (Figure 8a) and another at 3:22 p.m. on 13 July 2018 (Figure 8b).

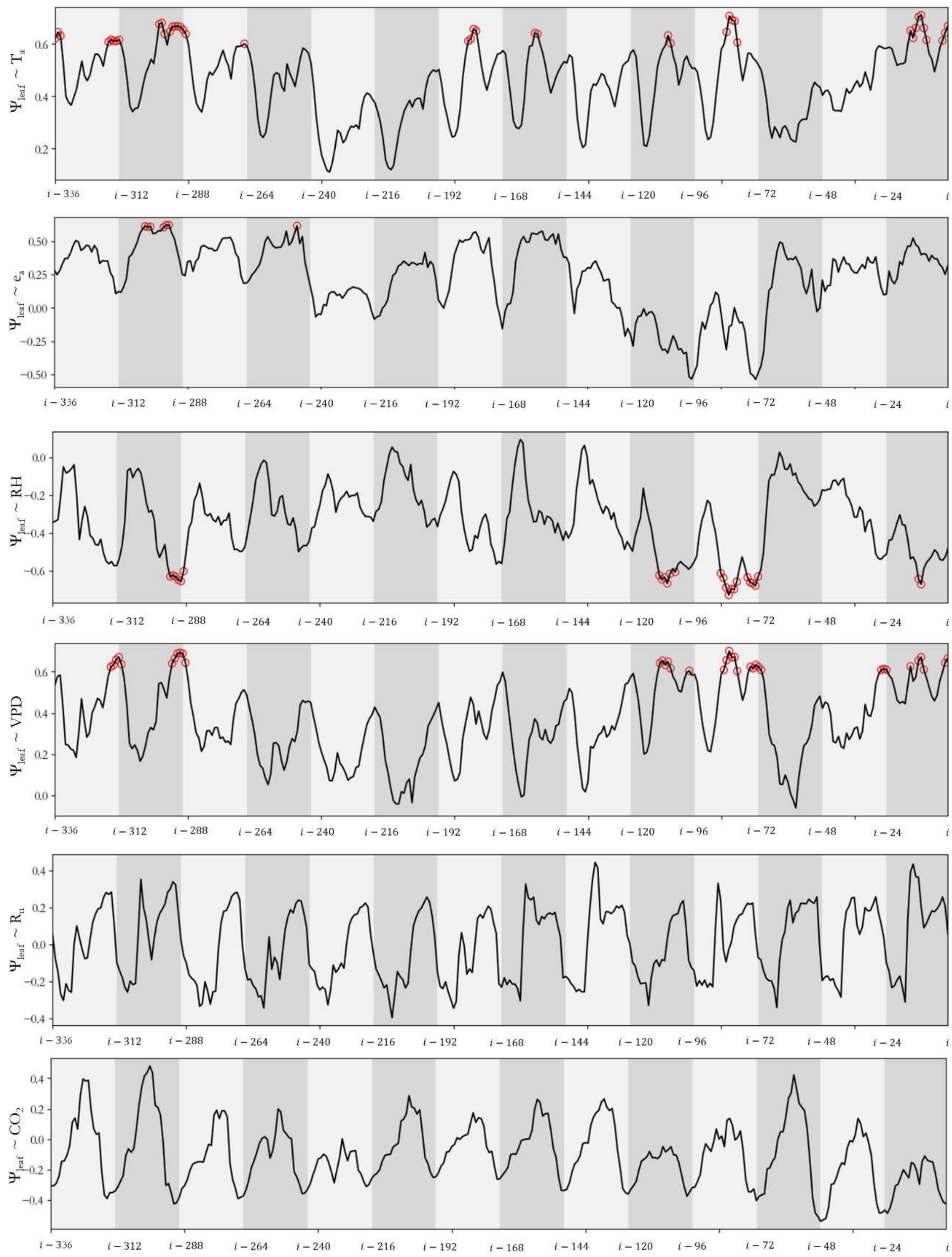

Figure 7. Pearson correlation coefficients between each meteorological and hour variable and measured Ψ_{leaf} across a 336-hour (14-day) historical window prior to flight time. The variable "i" denotes the hour of the sUAS flight, which occurred between 11 a.m. and 3 p.m., and "$i-336$" refers to 336 hours (14 days) before the flight. Each color block represents a 24-hour interval. The absolute correlation coefficients greater than 0.6 are highlighted with red cycles, indicating periods with stronger linear relationships between the meteorological variable and Ψ_{leaf}.

From these analyses, three representative features were derived for each variable:

(1) the value at the flight time, representing the condition during image acquisition and leaf water potential measurement; (2) the early-morning extreme (minimum for T_a and VPD, maximum for RH and CO_2 density), reflecting the initial physiological stress level and potential short-term weather trends; and (3) the difference between the flight-time value and its corresponding extreme, capturing the daytime change in meteorological conditions.

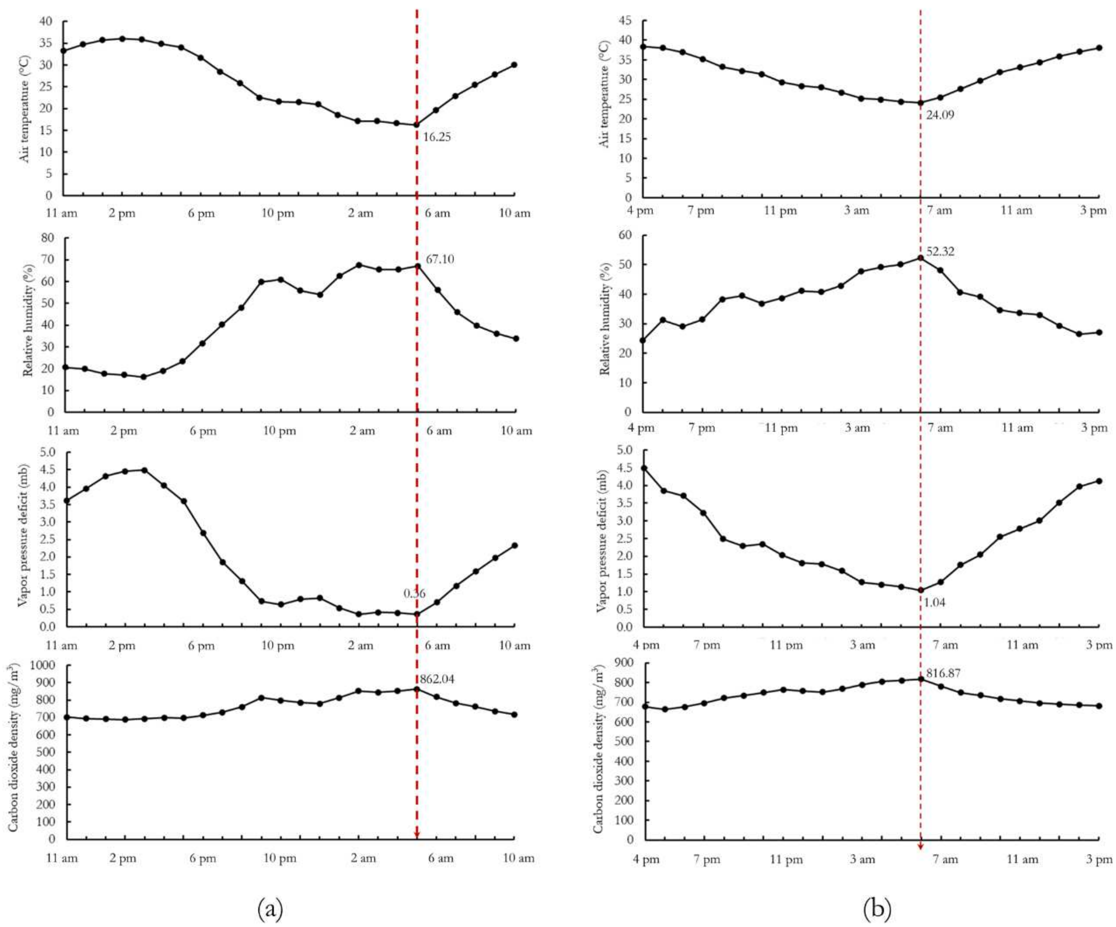

Figure 8. Example of the 24-hour variation in the four selected meteorological variables prior to sUAS data collection. Column(a) corresponds to the flight conducted at 10:41 a.m. on August 6th, 2018, while column (b) represents the flight at 3:22 p.m. on July 13th, 2018. The red dashed arrows indicate the approximate time of predawn, used to extract physiologically relevant extreme values for each variable.

3.2 Ψ_{leaf} estimation via XGB models and forward variable selection

The XGB model was initially developed using twenty input features, and its performance under this full-feature configuration (Table 2) served as the baseline. In Table 2, "Exp" denotes individual experiments, with the numeric suffix indicating the number of input variables included (e.g., "Exp 2" represents a model with two variables). The corresponding scatter plots are shown in Figure A 1. Air temperature (T_a) features included the flight-time value, the minimum value, and their difference, while canopy temperature (T_c) was derived from sUAS data.

A forward variable selection procedure was applied from Exp 1 to Exp 5. The process was intentionally stopped at Exp 5 to maintain model simplicity, with fewer than five input variables. In Exp 1, T_a (represented by the three derived features), was identified as the most influential predictor of Ψ_{leaf}, with model performance summarized in Table 2. However, because local meteorological sensors cannot capture spatial variability within the vineyard, subsequent variables were drawn from sUAS-derived data to improve spatial generalizability.

During Exp 2–Exp 5, the forward selection sequentially identified canopy temperature (T_c), the blue (B) spectral band, the red (R) band, and the simple ratio vegetation index (SR) as additional predictors.

Table 2. The performance for Ψ_{leaf} estimation using the XGB model for the testing tree records. "Exp" denotes "experiment". "Ta" represents three key temperature features: the temperature at the time of flight, the minimum temperature within a 24-hour period, and the temperature difference between these two values.

	RMSE	Bias	r	d	Features in the XGB model
Baseline	0.14	-0.06	0.88	0.91	All features were considered.
Exp 1	0.17	-0.08	0.81	0.85	T_a
Exp 2	0.16	-0.06	0.83	0.88	T_a, T_c
Exp 3	0.15	-0.05	0.84	0.89	T_a, T_c, B
Exp 4	0.15	-0.05	0.85	0.90	T_a, T_c, B, R
Exp 5	0.14	-0.06	0.88	0.91	T_a, T_c, B, R, SR

Table 3 provides a statistical assessment of the experiments shown in Table 2, evaluating whether the observed differences in mean performance are significant at the 5% level, assuming equal means across all groups under the null hypothesis.

Table 3. Comparing the mean value differences among different experiments using ANOVA and the Tukey test.

Group 1	Group 2	Mean Difference	p-Adj	Lower Boundary	Upper Boundary	Mean values are the same
Baseline	Exp 1	0.079	0.018	0.008	0.149	No
Baseline	Exp 2	-0.016	0.987	-0.087	0.055	Yes
Baseline	Exp 3	-0.026	0.903	-0.096	0.045	Yes
Baseline	Exp 4	-0.025	0.909	-0.096	0.045	Yes
Baseline	Exp 5	-0.023	0.942	-0.093	0.048	Yes

The results indicate that the null hypothesis of equal group means is rejected when only air temperature is considered. However, when both air temperature (three features) and canopy temperature are included, the hypothesis is not rejected. As additional variables are added, the hypothesis continues to be accepted across all subsequent experiments. These findings suggest that a model using only air temperature (three features) and canopy temperature (one feature) performs statistically equivalently to models incorporating all twenty features. Therefore, these four features, as defined in Table 2 and Table A 2, were retained for subsequent analyses.

The relative importance of the four selected features was evaluated using the "Gain" metric from the XGB model. Because the model was trained with RMSE as the objective function, "Gain" represents the average reduction in squared error achieved by splits using a particular feature within the decision trees. A higher Gain value, therefore, indicates greater contribution to reducing prediction error and higher relative importance in the model's predictive process.

Among the four predictors, canopy temperature showed the lowest importance (Gain = 0.36). In contrast, the minimum air temperature within the 24-hour period preceding the flight was the most influential (Gain = 8.14), followed by air temperature at flight time (Gain = 0.93) and the temperature difference between these two values (Gain = 0.79).

3.3 Ψ_{leaf} mapping and practice application

Ψ_{leaf} maps To assess spatial variability, Ψ_{leaf} maps of the RIP 720 vineyard were generated for three different times of day (Figure 9). The maps were produced using a simplified Python program (Gao et al., 2025), which implemented the methodology previously described in Section 2. The corresponding mean Ψ_{leaf} values ($\pm$ standard deviation) at 11:20, 13:17, and 15:38 were -1.10 ± 0.01 MPa, -1.15 ± 0.01 MPa, and -1.11 ± 0.01MPa, respectively.

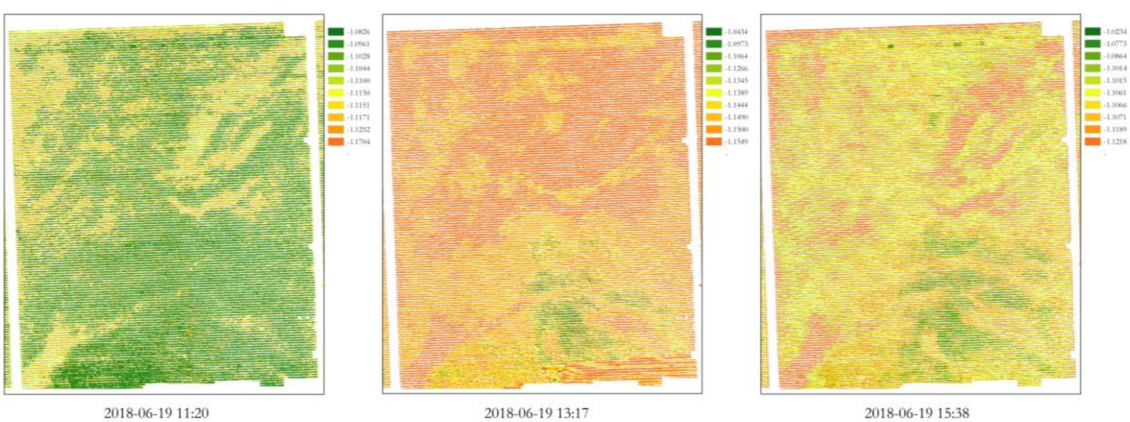

Figure 9. Estimated Ψ_{leaf} maps using Exp 2 inputs at different times on June 19, 2018 at RIP720.

As an additional validation for RIP 720, three Ψ_{leaf} measurements from a single vine location collected throughout the day on 19 June 2018 were excluded from XGB model training and later used to assess model performance (Table 4). The measured Ψ_{leaf} averaged -1.14 ± 0.05 MPa, while the modeled value was -1.12 ± 0.03 MPa. These results confirm that the XGB model can estimate Ψ_{leaf} with high accuracy and precision across different times of the day.

Notably, the lowest (most negative) Ψ_{leaf} value occurred at 13:17, followed by partial recovery by 15:38, despite continued increases in vapor pressure deficit (VPD). This diurnal pattern corresponded with a decline in the Bowen ratio, indicating a gradual shift in surface energy partitioning toward latent heat flux. Such behavior suggests active stomatal regulation and transpiration adjustment under sustained atmospheric demand. Collectively, these observations imply that Ψ_{leaf} dynamics are governed not only by external atmospheric forcing but also by vine-level physiological feedback mechanisms.

Table 4. The Ψ_{leaf} measurements and the corresponding XGB modeled Ψ_{leaf} at one single location within the RIP 720 vineyard throughout the day on June 19, 2018. The local VPD measurements, latent heat flux, sensible heat flux, and the corresponding Bowen ratio were also provided.

Time	Measured (MPa)	Modeled (MPa)	VPD (kPa)	Latent heat flux (Wm-2)	Sensible heat flux (Wm-2)	Bowen ratio
11:20	-1.08	-1.10	~2.43	~402.57	~100.90	~0.25
13:17	-1.20	-1.15	~2.92	~409.66	~86.44	~0.21
15:38	-1.15	-1.10	~3.06	~318.47	~14.74	~0.05

Given the geographical proximity of the RIP 720 and RIP 760 vineyards, multispectral imagery for RIP 760 was acquired simultaneously using AggieAir. However, Ψ_{leaf} measurements for RIP 760 were not available in this study. In addition, differences in grapevine variety and vineyard management practices introduce further variability between these two vineyards. Figure A 2 presents Ψ_{leaf} maps for RIP 760 at the same three flight times, allowing for a comparison based solely on remotely sensed data.

Despite these site-specific differences, both vineyards exhibited similar diurnal trends, with the most negative Ψ_{leaf} values occurring at 13:17, reflecting peak plant water stress during midday. These findings highlight the potential of meteorological and remote sensing-driven machine learning models to capture the dynamics of plant water status across vineyards with varying conditions.

4. Discussion

This study demonstrates the feasibility of using a reduced feature set derived from sUAS imagery and short-term meteorological data to estimate grapevine Ψ_{leaf} across commercial vineyards. The modeling framework was deliberately designed for operational simplicity to support near-real-time crop water stress monitoring and precision irrigation. While some meteorological variables recorded several days prior to the flight exhibited an interesting correlation with Ψ_{leaf}, in this study, we restricted our analysis to the 24-hour period preceding each UAV flight.

This choice was motivated by two key considerations. First, maintaining a 24-hour window allowed us to pair meteorological conditions with the specific time of observation directly, ensuring more straightforward model interpretability and comparability (meteorological conditions at pre-dawn have an influence on stress conditions during the day). Second, the 24-hour window aligns with the intended goal of building a practical, transferable model for operational use. While the observed influence of meteorological conditions from prior days suggests that physiological time-lag effects may exist, these dynamics are not yet fully understood and were beyond the scope of this study. Additionally, although meteorological variables from earlier days (e.g., 13 days before the flight) showed high correlations with Ψ_{leaf}, their inclusion posed challenges. Due to the lack of consistent physiological evidence defining the appropriate time-lag structure and the variability in sampling times across sites and seasons, such long-range predictors may introduce noise and overfitting, especially when generalizing to new fields or crops. As such, we prioritized temporal proximity and consistency to support practical deployment and model transferability. Future research should explore more sophisticated approaches to investigate the effects of long-term meteorological time-lags on grapevine Ψ_{leaf}, particularly to better understand underlying physiological mechanisms and improve model interpretability.

For this study, key meteorological variables were selected based on the extreme value — either the maximum or minimum — obtained from the 24-hour historical records, as all variables reached their respective extremes simultaneously. This synchronous occurrence provided a consistent representation of atmospheric conditions during the observed time window. Based on recent research findings, future studies are encouraged to examine the effects of both minimum and maximum extremes on Ψ_{leaf} to better capture the full range of plant physiological responses. Furthermore, given that publicly available meteorological datasets commonly include both maximum and minimum air temperature, there is a promising opportunity to scale these findings to broader spatial extents. This could be achieved by combining remote sensing data (e.g., 30-meter Landsat multispectral imagery) with gridded meteorological datasets (e.g., California Irrigation Management Information System – CIMIS) to evaluate drought conditions from an alternative and complementary perspective. Future research should also explore the feasibility of leveraging high-resolution imagery ($\leq$ 1 m pixel) to inform drought or vegetation stress assessments using coarser-resolution meteorological and remote sensing datasets.

Regarding the XGB model, the Feature importance was assessed using the "Gain" metric. While this metric offers valuable insights, it may not fully capture complex, nonlinear interactions among variables. Two additional importance metrics, Weight (frequency of use in splits) and Cover (the number of samples affected by a split), can provide complementary perspectives on feature influence. Furthermore, advanced interpretation methods such as SHAP (SHapley Additive exPlanations) values can also be used for the understanding of both global and local feature contributions. Incorporating these tools in future analyses could enhance feature selection and model interpretability by uncovering intricate dependencies and interactions between meteorological variables and image-derived predictors associated with Ψ_{leaf}, while maintaining the overall goal of operational simplicity.

Although the estimated Ψ_{leaf} maps for both RIP 720 and RIP 760 vineyards exhibited discernible spatial patterns, they also revealed a characteristic uniformity in the estimated Ψ_{leaf} values within specific areas. This observation provided valuable insights for handling Ψ_{leaf} sample extensions. The method described in Section 2.4 allows for generating additional samples for machine learning, but inherently reduces the variability captured by the sUAS data. Specifically, the machine learning model assigns a single measured Ψ_{leaf} value to represent each 0.6-meter pixel within the rectangular domain, thereby forcing the variability in the sUAS data to become uniform. Therefore, using smaller domains in future studies may help mitigate the uniformity issue and preserve the inherent variability in the data.

While our model was successfully tested in an independent vineyard with different cultivars and management practices, further work is needed to assess its performance in vineyards with greater environmental or geographic diversity. Integrating additional data types, such as soil moisture, plant phenology, or irrigation schedules, could further improve generalizability and predictive power. Extending the model to different regions or crops could also validate its broader applicability in precision agricultural water management.

5. Conclusions

In this study, we developed a machine learning framework to estimate grapevine Ψ_{leaf} by integrating time-series meteorological data with sUAS-derived canopy observations, focusing on the 24-hour period preceding data collection to enhance operational relevance and real-time applicability. By leveraging key features (predictors), including maximum air temperature, flight-time air temperature, their temperature difference, and canopy temperature, our XGB model achieved estimative accuracy at RMSE = 0.16 MPa, bias = –0.06 MPa, and r = 0.83, while maintaining computational efficiency. The estimated Ψ_{leaf} maps and statistical summaries effectively captured diurnal water stress dynamics, with peak stress occurring around midday. Importantly, the model demonstrated strong generalizability across vineyards with distinct environmental and geographic conditions, highlighting its potential for scalable deployment in commercial settings. While localized uniformity in some estimated Ψ_{leaf} values indicated a potential need for more granular field measurements, this work provides a robust foundation for advancing vineyard water stress monitoring. Future refinements in model architecture (both feature extraction and machine learning models) and input resolution can potentially further enhance precision irrigation strategies and improve resilience in water-limited viticulture systems. Moreover, insights from this field-scale research can serve as a critical foundation for scaling up to regional drought assessment and adaptive water management across broader agricultural landscapes.

Appendix

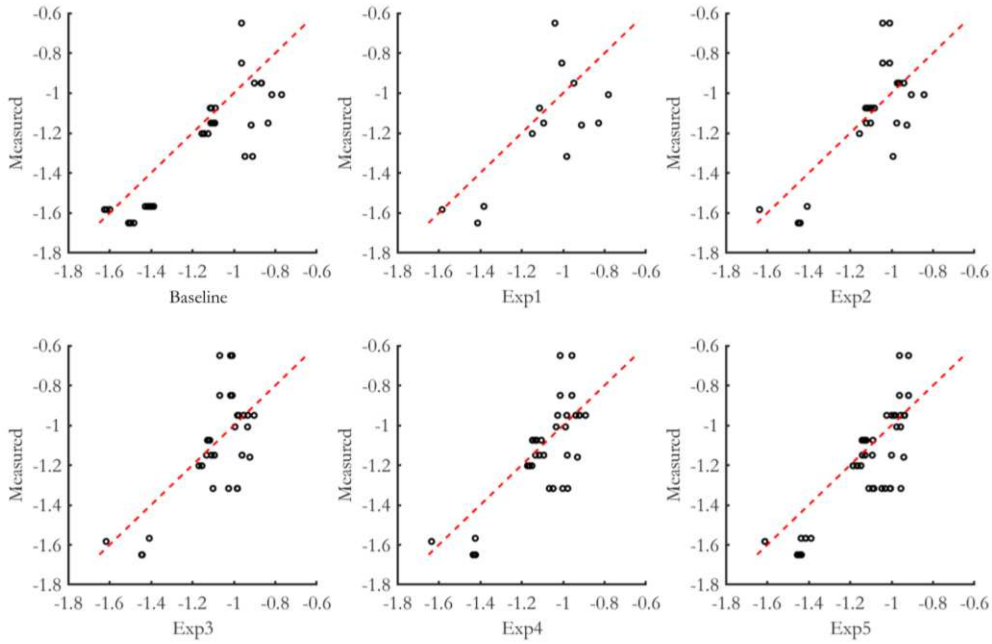

Figure A 1. Scatter plots showing the XGB model performance corresponding to Table 2.

Table A 1. The XGB model performance under different scenarios.

Inputs for the XGB model	RMSE	Bias	r	d
Only considering inputs from the meteorological data	0.17	-0.08	0.82	0.86
Only considering inputs from sUAS	0.20	-0.03	0.67	0.79
Considering both types of inputs	0.14	-0.06	0.88	0.91

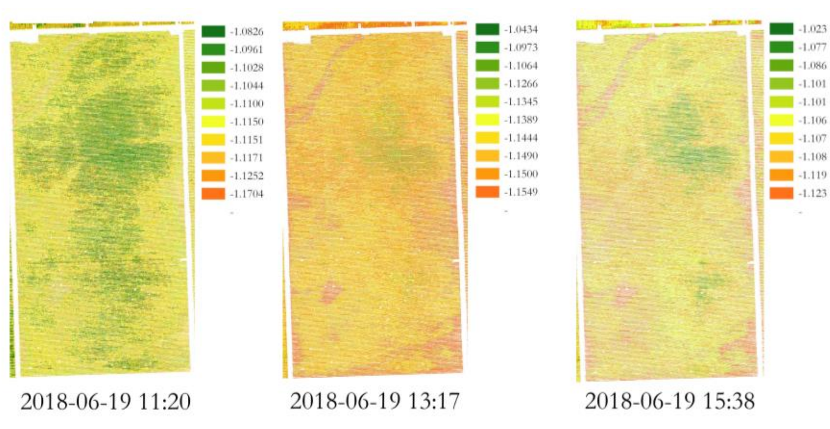

Figure A 2. Estimated Ψ_{leaf} maps at different times on the same day at RIP760.

Table A 2. Twenty features used in the XGB model as the baseline.

Variable name	Description	Variable name	Description
R	Red spectral band	VPD_diff	The corresponding vapor pressure deficit between the previous two values
G	Green spectral band	Ta_min	Minimum air temperature
B	Blue spectral band	Ta_fly	Air temperature at flight time
NIR	Near-infrared spectral band	Ta_diff	The corresponding air temperature difference between the previous two values
NDVI	Normalized difference vegetation index	RH_max	The maximum relative humidity
SAVI	Soil-adjusted vegetation index	RH_fly	Relative humidity at flight time
SR	Simple ratio	RH_diff	The corresponding relative humidity difference between the previous two values
Tc	Canopy temperature	CO_2_max	The maximum carbon dioxide density
VPD_min	Minimum vapor pressure deficit	CO_2_fly	Carbon dioxide density at flight time
VPD_fly	Vapor pressure deficit at flight time	CO_2_diff	The corresponding carbon dioxide density difference between the previous two values

Acknowledgements

This study was made possible with financial support from the USDA-Agricultural Research Service, E&J Gallo Winery, and the Utah Water Research Laboratory Student Fellowship. The authors are also grateful for the extraordinary support from the Utah State University AggieAir sUAS program staff and the E&J Gallo scientific teams for data collection and analysis and the cooperation of the vineyard management staff for logistical support and coordinating field operations with the GRAPEX team. The authors would like to thank Carri Richards for editing the manuscript. Mention of trade names or commercial products in this publication is solely for the purpose of providing specific information and does not imply recommendation or endorsement by the US Department of Agriculture. USDA is an equal opportunity provider and employer.

Funding Declaration

Funds for this study were provided by the USDA USU NACA grants, with data collected by previous NASA grant. Student support was provided by the graduate assistantship at the Utah Water Research Laboratory.

Reference

Abbatantuono, F., Lopriore, G., Tallou, A., Brillante, L., Ali, S. A., Camposeo, S., & Vivaldi, G. A. (2024). Recent progress on grapevine water status assessment through remote and proximal sensing: A review. *Scientia Horticulturae*, *338*, 113658. https://doi.org/10.1016/J.SCIENTA.2024.113658

Aboutalebi, M., Torres-Rua, A. F., McKee, M., Kustas, W. P., Nieto, H., Alsina, M. M., White, A., Prueger, J. H., McKee, L., Alfieri, J., Hipps, L., Coopmans, C., & Dokoozlian, N. (2019). Incorporation of Unmanned Aerial Vehicle (UAV) Point Cloud Products into Remote Sensing Evapotranspiration Models. *Remote Sensing*, *12*(1), 50. https://doi.org/10.3390/rs12010050

Albrizio, R., Puig-Sirera, Sellami, M. H., Guida, G., Basile, A., Bonfante, A., Gambuti, A., & Giorio, P. (2023). Water stress, yield, and grape quality in a hilly rainfed "Aglianico" vineyard grown in two different soils along a slope. *Agricultural Water Management*, *279*, 108183. https://doi.org/10.1016/J.AGWAT.2023.108183

Alliaume, F., Echeverria, G., Ferrer, M., & González Barrios, P. (2024). A Study of the Multivariate Spatial Variability of Soil Properties, and their Association with Vine Vigor Growing on a Clayish Soil. *Journal of Soil Science and Plant Nutrition*, *24*(2), 3282–3297. https://doi.org/10.1007/s42729-024-01751-8

Bonada, M., & Sadras, V. O. (2015). Review: Critical appraisal of methods to investigate the effect of temperature on grapevine berry composition. In *Australian Journal of Grape and Wine Research* (Vol. 21, Issue 1, pp. 1–17). https://doi.org/10.1111/ajgw.12102

Bravdo, B., Hepner, Y., Loinger, C., Cohen, S., & Tabacman, H. (1985). Effect of Irrigation and Crop Level on Growth, Yield and Wine Quality of Cabernet Sauvignon. *American Journal of Enology and Viticulture*, *36*(2), 132–139. https://doi.org/10.5344/AJEV.1985.36.2.132

Chaves, M. M., Zarrouk, O., Francisco, R., Costa, J. M., Santos, T., Regalado, A. P., Rodrigues, M. L., & Lopes, C. M. (2010). Grapevine under deficit irrigation: hints from physiological and molecular data. In *Annals of botany* (Vol. 105, Issue 5, pp. 661–676). https://doi.org/10.1093/aob/mcq030

Diffenbaugh, N. S., White, M. A., Jones, G. V., & Ashfaq, M. (2011). Climate adaptation wedges: A case study of premium wine in the western United States. *Environmental Research Letters*, *6*(2). https://doi.org/10.1088/1748-9326/6/2/024024

Ferro, M. V., Catania, P., Miccichè, D., Pisciotta, A., Vallone, M., & Orlando, S. (2023). Assessment of vineyard vigour and yield spatio-temporal variability based on UAV high resolution multispectral images. *Biosystems Engineering*, *231*, 36–56. https://doi.org/10.1016/j.biosystemseng.2023.06.001

Gao, R. (2025). Goodness of Fit Model. In *Zenodo*. Zenodo. https://doi.org/10.5281/zenodo.16700596

Gao, R., & Torres-Rua, A. (2025). *Feature extraction from the high-resolution AggieAir images for leaf water potential estimation in California vineyards*. Zenodo. https://doi.org/https://doi.org/10.5281/zenodo.16730652

Gao, R., Torres-Rua, A., & Alsina, M. M. (2025). *A simplified model for California grapevine leaf water potential mapping at the field scale based on a machine learning approach*. Zenodo. https://doi.org/https://doi.org/10.5281/zenodo.15885589

Gao, R., & Torres-Rua, A. F. (2023). *Temperature separation via eliminating shadow-pixel influence based on high-resolution sUAS image in California vineyards* (p. 4). CUAHSI HydroShare. https://doi.org/https://doi.org/10.4211/hs.c0876501581f46c698727dc956cc2d73

Gao, R., Torres-Rua, A. F., Aboutalebi, · Mahyar, White, W. A., Anderson, M., Kustas, W. P., Agam, N., Alsina, M. M., Alfieri, · Joseph, Hipps, L., Dokoozlian, · Nick, Nieto, · Hector, Feng Gao, ·, Lynn, ·, Mckee, G., Prueger, J. H., Luis Sanchez, ·, Mcelrone, A. J., Bambach-Ortiz, N., … Gowing, I. (2022). LAI estimation across California vineyards using sUAS multi-seasonal multi-spectral, thermal, and elevation information and machine learning. *Irrigation Science 2022*, *1*, 1–29. https://doi.org/10.1007/S00271-022-00776-0

Gao, R., Torres-Rua, A. F., Nassar, A., Alfieri, J., Aboutalebi, M., Hipps, L., Ortiz, N. B., Mcelrone, A. J., Coopmans, C., Kustas, W., White, W., McKee, L., del Mar Alsina, M., Dokoozlian, N., Sanchez, L., Prueger, J. H., Nieto, H., & Agam, N. (2021). *Evapotranspiration partitioning assessment using a machine-learning-based leaf area index and the two-source energy balance model with sUAV information* (J. A. Thomasson & A. F. Torres-Rua, Eds.; Vol. 11747, Issue 12, p. 21). SPIE. https://doi.org/10.1117/12.2586259

Gao, R., Torres-Rua, A. F., Nieto, H., Zahn, E., Hipps, L., Kustas, W. P., Alsina, M. M., Bambach, N., Castro, S. J., Prueger, J. H., Alfieri, J., McKee, L. G., White, W. A., Gao, F., McElrone, A. J., Anderson, M., Knipper, K., Coopmans, C., Gowing, I., … Dokoozlian, N. (2023). ET

Partitioning Assessment Using the TSEB Model and sUAS Information across California Central Valley Vineyards. *Remote Sensing*, *15*(3), 756. https://doi.org/10.3390/RS15030756

Grantham, T. E., & Viers, J. H. (2014). 100 years of California's water rights system: Patterns, trends and uncertainty. *Environmental Research Letters*, *9*(8). https://doi.org/10.1088/1748-9326/9/8/084012

Hannah, L., Roehrdanz, P. R., Ikegami, M., Shepard, A. V., Shaw, M. R., Tabor, G., Zhi, L., Marquet, P. A., & Hijmans, R. J. (2013). Climate change, wine, and conservation. *Proceedings of the National Academy of Sciences of the United States of America*, *110*(17), 6907–6912. https://doi.org/10.1073/pnas.1210127110

Kustas, W. P., Agam, N., & Ortega-Farias, S. (2019). Forward to the GRAPEX special issue. *Irrigation Science*, *37*(3), 221–226. https://doi.org/10.1007/s00271-019-00633-7

Kustas, W. P., Anderson, M. C., Alfieri, J. G., Knipper, K., Torres-Rua, A., Parry, C. K., Nieto, H., Agam, N., White, W. A., Gao, F., McKee, L., Prueger, J. H., Hipppps, L. E., Los, S., Alsina, M. M., Sanchez, L., Sams, B., Dokoozlian, N., McKee, M., … Hain, C. (2018). The Grape Remote Sensing Atmospheric Profile and Evapotranspiration Experiment. *Bulletin of the American Meteorological Society*, *99*(9), 1791–1812. https://doi.org/10.1175/BAMS-D-16-0244.1

Laroche-Pinel, E., Vasquez, K. R., & Brillante, L. (2024). Assessing grapevine water status in a variably irrigated vineyard with NIR/SWIR hyperspectral imaging from UAV. *Precision Agriculture*, 1–19. https://doi.org/10.1007/S11119-024-10170-9/FIGURES/7

Miras-Avalos, J. M., & Araujo, E. S. (2021). Optimization of Vineyard Water Management: Challenges, Strategies, and Perspectives. *Water 2021, Vol. 13, Page 746*, *13*(6), 746. https://doi.org/10.3390/W13060746

Mitchell, J. P., Carter, L. M., Reicosky, D. C., Shrestha, A., Pettygrove, G. S., Klonsky, K. M., Marcum, D. B., Chessman, D., Roy, R., Hogan, P., & Dunning, L. (2016). A history of tillage in California's Central Valley. In *Soil and Tillage Research* (Vol. 157, pp. 52–64). Elsevier. https://doi.org/10.1016/j.still.2015.10.015

Nassar, A., Torres-rua, A., Kustas, W., Alfieri, J., Hipps, L., Prueger, J., Nieto, H., Alsina, M. M., White, W., McKee, L., Coopmans, C., Sanchez, L., & Dokoozlian, N. (2021). Assessing daily evapotranspiration methodologies from one-time-of-day suas and ec information in the grapex project. *Remote Sensing*, *13*(15), 2887. https://doi.org/10.3390/rs13152887

Nicholas, K. A., & Durham, W. H. (2012). Farm-scale adaptation and vulnerability to environmental stresses: Insights from winegrowing in Northern California. *Global Environmental Change*, *22*(2), 483–494. https://doi.org/10.1016/j.gloenvcha.2012.01.001

Poblete, T., Ortega-Farías, S., Moreno, M. A., & Bardeen, M. (2017). Artificial neural network to predict vine water status spatial variability using multispectral information obtained from an unmanned aerial vehicle (UAV). *Sensors (Switzerland)*, *17*(11). https://doi.org/10.3390/s17112488

Sperry, J. S. (2000). Hydraulic constraints on plant gas exchange. In *Agricultural and Forest Meteorology* (Vol. 104).

Tang, Z., Jin, Y., Alsina, M. M., McElrone, A. J., Bambach, N., & Kustas, W. P. (2022). Vine water status mapping with multispectral UAV imagery and machine learning. *Irrigation Science*, *40*(4–5), 715–730. https://doi.org/10.1007/S00271-022-00788-W

Viers, J. H., Williams, J. N., Nicholas, K. A., Barbosa, O., Kotzé, I., Spence, L., Webb, L. B., Merenlender, A., & Reynolds, M. (2013). Vinecology: Pairing wine with nature. In *Conservation Letters* (Vol. 6, Issue 5, pp. 287–299). https://doi.org/10.1111/conl.12011

Williams, L. E., & Araujo, F. J. (2002). Correlations among Predawn Leaf, Midday Leaf, and Midday Stem Water Potential and their Correlations with other Measures of Soil and Plant Water Status in Vitis vinifera. *Journal of the American Society for Horticultural Science*, *127*(3), 448–454. https://doi.org/10.21273/JASHS.127.3.448

Willmott, C. J. (1982). Some comments on the evaluation of model performance. *Bulletin - American Meteorological Society*, *63*(11), 1309–1313. https://doi.org/10.1175/1520-0477(1982)063<1309:SCOTEO>2.0.CO;2